Journal Pre-proof

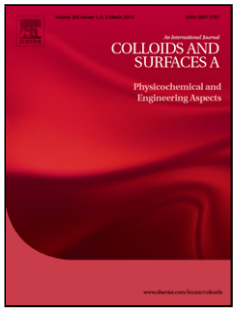

Novel magnetic nanocomposite of calcium alginate carrying poly(pyrimidine-thiophene-amide) as a novel green synthesized polyamide for adsorption study of neodymium, terbium, and dysprosium rare-earth ions

Hamedreza Javadian, Montserrat Ruiz, Mehdi Taghvai, Ana Maria Sastre

PII: S0927-7757(20)30845-1

DOI: https://doi.org/10.1016/j.colsurfa.2020.125252

Reference: COLSUA 125252

To appear in: *Colloids and Surfaces A: Physicochemical and Engineering Aspects*

Received Date: 4 May 2020

Revised Date: 28 June 2020

Accepted Date: 29 June 2020

Please cite this article as: Javadian H, Ruiz M, Taghvai M, Sastre AM, Novel magnetic nanocomposite of calcium alginate carrying poly(pyrimidine-thiophene-amide) as a novel green synthesized polyamide for adsorption study of neodymium, terbium, and dysprosium rare-earth ions, *Colloids and Surfaces A: Physicochemical and Engineering Aspects* (2020), doi: https://doi.org/10.1016/j.colsurfa.2020.125252

Novel magnetic nanocomposite of calcium alginate carrying poly(pyrimidine-thiophene-amide) as a novel green synthesized polyamide for adsorption study of neodymium, terbium, and dysprosium rare-earth ions

Hamedreza Javadian[a,*], Montserrat Ruiz[b], Mehdi Taghvai[c], Ana Maria Sastre[a]

[a] Department of Chemical Engineering, ETSEIB, Universitat Politècnica de Catalunya, Diagonal 647, 08028 Barcelona, Spain

[b] Department of Chemical Engineering, EPSEVG, Universitat Politècnica de Catalunya, Av. Víctor Balaguer, s/n, 08800 Vilanova i la Geltrú, Spain

[c] Department of Chemistry, Faculty of Science, Shahid Chamran University of Ahvaz, 61357-43337, Iran

[*]Corresponding author.

Email addresses: Hamedreza.javadian@yahoo.com; Hamedreza.javadian@upc.edu

Graphical abstract

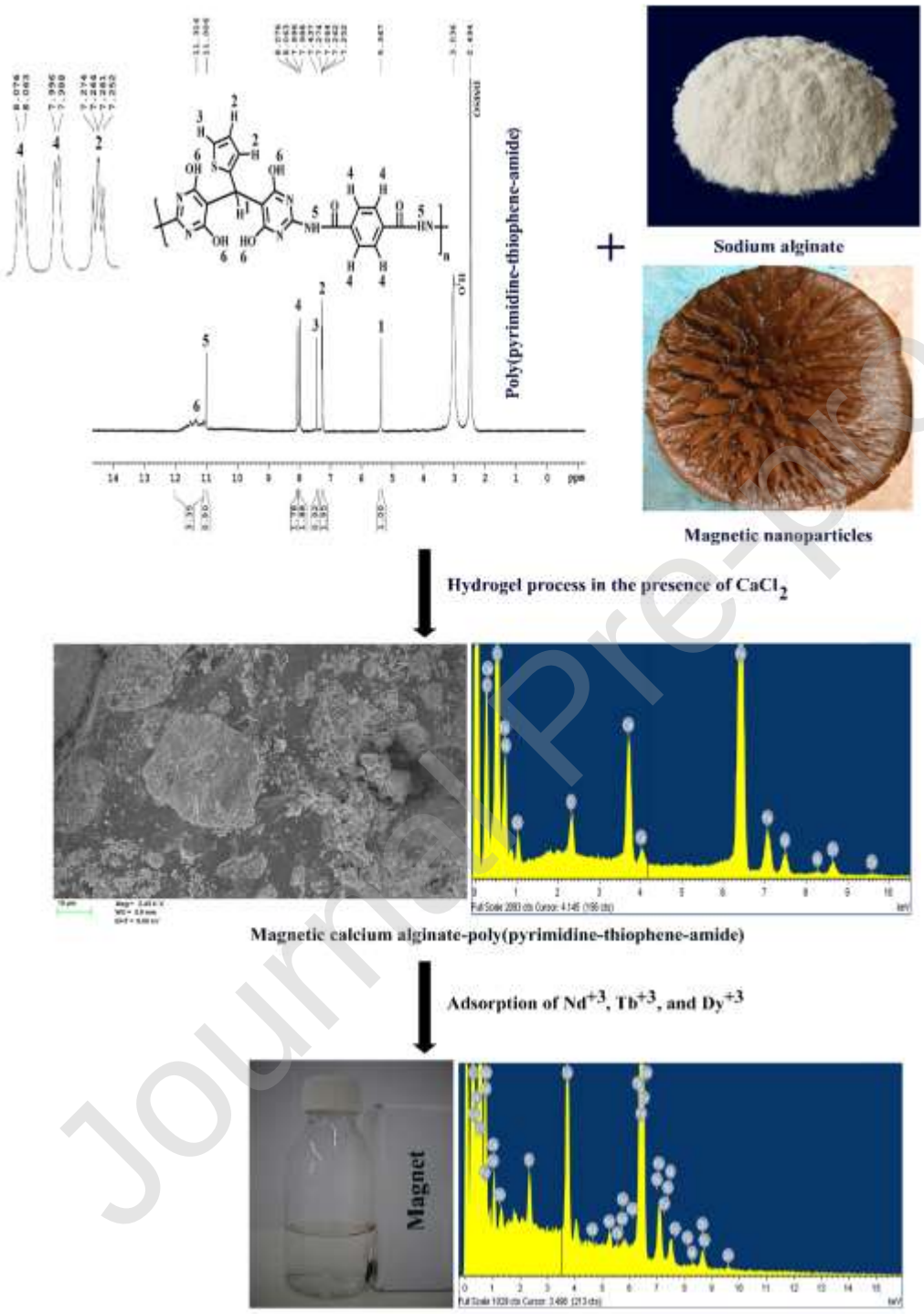

Highlights

- Synthesis of a novel polyamide containing pyrimidine and methine thiophene linkages.
- NMR analysis for the confirmation of P(P-T-A) synthesis.
- Synthesis of the magnetic calcium alginate/P(P-T-A).
- Saturation magnetization of 15.28 emu/g for the nanocomposite.
- Well-fitting of the REEs adsorption data by pseudo-second-order model.

Abstract

In this paper, a novel polyamide containing pyrimidine and methine thiophene linkages (poly(pyrimidine-thiophene-amide) (P(P-T-A))) was synthesized. Then, the magnetic calcium alginate nanocomposite containing P(P-T-A) (CA-P(P-T-A)-$Ni_{0.2}Zn_{0.2}Fe_{2.6}O_4$ (NZFO)) was synthesized for studying neodymium (Nd^{+3}), terbium (Tb^{+3}), and dysprosium (Dy^{+3}) ions adsorption in the single ion solutions. The obtained results of X-ray diffraction (XRD), field emission scanning electron microscope (FE-SEM), energy-dispersive X-ray (EDX), nuclear magnetic resonance (NMR), thermogravimetric analysis (TGA), vibrating sample magnetometer (VSM), and Fourier transform infrared (FT-IR) indicated the successful synthesis of the materials. The value of saturation magnetization of the nanocomposite was reported to be 15.28 emu/g, indicating an appropriate magnetic response. Under the optimum conditions, adsorption efficiency for Nd^{+3}, Tb^{+3}, and Dy^{+3} was 96.73, 94.82, and 97.58 %, respectively. According to the experimental results, it can be stated that the data of REEs adsorption were efficiently fitted by nonlinear pseudo-second-order kinetic model. Adsorption isotherms were also evaluated by fitting with Freundlich and Langmuir isotherm models. A better fit was achieved by Freundlich model in the case of Tb^{+3} and Dy^{+3} ions, while Langmuir isotherm fitting reported a better result

for Nd^{+3} adsorption data. Moreover, the changes in Gibbs free energy (ΔG°), enthalpy (ΔH°), and entropy (ΔS°) values presented a feasible and endothermic ions adsorption process onto the nanocomposite that occurred spontaneously under the investigated conditions. The obtained results indicated that the nanocomposite can be considered as a potential adsorbent for the efficient adsorption of the investigated ions.

Keywords: Poly(pyrimidine-thiophene-amide), Calcium alginate, Magnetic, Nanocomposite, Adsorption, Rare-earth ions.

1. Introduction

In recent years, the extensive utilization of rare earth elements (REEs) in numerous innovative implements such as TVs, laser, liquid crystal displays (LCDs), screens, fluorescent lamps, particular magnets, etc., has been reported by researchers [1-3]. Owing to concentration on the extraction of REEs in a couple of nations, especially China, western countries consider the recycling of REEs as a vital issue. After publishing a report by the European Commission in 2010 concerning the definition of fourteen elements, including REEs, as critical elements for EU economy, attentions have been heightening for gathering and recycling wastes that contain such critical elements, and numerous mandates have been forced to back up these goals in the EU-27 [4].

The aforementioned reasons clarify why recycling the wastes of electrical and electronic equipment (WEEE) and particular magnets is receiving growing consideration. Besides, the quantity of such wastes created in western nations is not only enormous but also develops yearly. Thus, a real secondary mine, known as urban mine, is represented for the recovery of base, precious, and rare earth elements [5].

In this manner, various techniques have been carried out for REEs recovery such as co-precipitation, solvent extraction, ion exchange, hydrometallurgy, adsorption, and so on [6]. It is noticeable that adsorption has been demonstrated to be a highly applicable method for the treatment of water containing ions because of being an uncomplicated operation, highly efficient, and cost-effective [7]. So far, a variety of adsorbents such as resin, inorganic nanoparticles, biomaterials, and functional polymeric materials have been applied for recovering REEs and heavy metals [8,9]. The low adsorption capacity of the adsorbents is one of the reasons that motivates investigators to synthesis alternative adsorbents with better performance.

Alginate, as a natural polymer, is the derivation of various types of brown algae. The properties of alginate such as biocompatibility, low cost, and capability of carboxyl groups of alginate for the formation of complexes with ions such as cobalt alginate (Co-Alg_2), nickel alginate (Ni-Alg_2), and copper alginate (Cu-Alg_2) make it as a potential adsorbent [10]. The transformation of alginate aqueous solution into hydrogel can be taken place by adding metallic divalent cations. Numerous researches have reported the important role of the porous structure of ionotropic metal alginates for metal ions adsorption from aqueous media [11].

Polyamides (PAs), known as one of polymeric materials possessing high performance, are commonly characterized by high melting point, good mechanical properties, good chemical resistance, and thermo-oxidative stability that are gathered all together to provide an extensive range of applications [12,13]. During recent years, many researchers have tried to use several procedures to enhance the processability of PAs using structural modification without any negative effects on their remarkable chemical, mechanical, and thermal properties in order to retain aromatic PAs application at the center of scientific research. The introduction of heteroaromatic rings, aliphatic parts, cardo moieties, bulky pendant groups, and non-coplanar

structural segments in the polymer backbone not only prevents their alignment and interrupts the hydrogen bonding but also enhances their processability [14].

Ionic Liquids (ILs) are considered as low melting salts that demonstrate a new kind of advanced and technological ionic solvents that can be considered to be used in a specific application [15,16]. Studying the dialkylimidazolium based ILs has gained substantial attention as promising alternative green solvents and catalysts in polymer synthesis. Hence, they have been considerably expanded, and consequently, a various number of alternatives are accessible or even commercially available. There have been numerous reports on the effective formation of PAs with high molecular weight by the polycondensation processes in ILs [17].

In the present study, calcium alginate/(poly(pyrimidine-thiophene-amide)/$Ni_{0.2}Zn_{0.2}Fe_{2.6}O_4$ (CA/P(P-T-A)/NZFO) was synthesized by the gelation process of sodium alginate in the presence of P(P-T-A) and NZFO and then used as a novel adsorbent for the REEs adsorption. XRD, FE-SEM, EDX, NMR, TGA, VSM, and FT-IR were the methods utilized for characterizing the synthesized materials. To reach the conditions for optimum adsorption, pH, adsorbent dosage, contact time, ionic strength, and initial concentration of the REEs as effective parameters on adsorption process were investigated. Fitting the data of REEs adsorption by the kinetic and isotherm models were performed, and to test the reusability of CA/P(P-T-A)/NZFO, four cycles of adsorption-desorption were experimented.

2. Materials and methods

2.1. Materials and reagents

Sodium alginate was bought from PanReac AppliChem. $Dy(NO_3)_3.5H_2O$ was provided by Alfa Aesar. $Fe(NO_3)_3.9H_2O$, $Nd(NO_3)_3.6H_2O$, $Zn(NO_3)_2.6H_2O$, $Tb(NO_3)_3{\cdot}6H_2O$, $Ni(NO_3)_2{\cdot}6H_2O$, triphenyl phosphite (TPP), 2-amino-4,6-dihydroxypyrimidine, terephthalic acid,

glutaraldehyde, dimethyl sulfoxide (DMSO), 2-thiophenecarboxaldehyde, and methanol were bought from Sigma-Aldrich. Each salt was dissolved in deionized water (DW) to prepare the stock solution of 1000 mg/L for each ion. HNO_3 or NaOH with the concentration of 0.1 M was utilized for pH adjustment.

2.2. Synthesis of $Ni_{0.2}Zn_{0.2}Fe_{2.6}O_4$ magnetic nanoparticles

$Ni_{0.2}Zn_{0.2}Fe_{2.6}O_4$ magnetic nanoparticles were synthesized by hydrothermal method. A mixed solution of 0.2 M Ni^{2+}, 0.2 M Zn^{2+} and 2.6 M Fe^{3+} was prepared in HCl solution, and then NaOH solution was added into the mixed solution under nitrogen gas, and pH of the mixture was adjusted to 10.5. To this mixture, 0.3 g of CTAB was added, and then it was placed into an autoclave (Teflon-lined stainless steel) at 200 $^{\circ}$C of an oven for 8 h for hydrothermal treatment. In the following, the temperature of the autoclave was naturally decreased to the room temperature (RT), and the precipitate was collected and rinsed several times using DW to reach neutral pH. Finally, the obtained particles were dried at 50 $^{\circ}$C.

2.3. Ionic liquid synthesis

The RT Ionic Liquid (IL) was synthesized based on the procedure introduced in the literature [18].

2.4. Synthesis of 5,5' -(thiophene-2- ylmethylene)bis(2-aminopyrimidine-4,6-diol) (TMAPD)

TMAPD was synthesized according to the following procedure: A mixture containing 2.54 g (0.02 mol) of 2-amino-4,6-dihydroxypyrimidine, 1 mL (0.01 mol) of 2-thiophenecarboxaldehyde, and 20 mL of DMSO was stirred for 6 h at 110 $^{\circ}$C. After completion of the reaction tested by thin-layer chromatography, the temperature of the solution was decreased to the RT, and a violet powder obtained by pouring the solution into 400 mL of cold DW (-5 $^{\circ}$C) was filtered, rinsed several times using DW and then dried using vacuum oven at

100 °C. The reaction yield was 92 % (3.20 g), and the obtained compound has not shown sharp melting point and started to be decomposed above 300 °C. FT-IR (KBr, cm^{-1}): 3153-3477 (stretching of O-H and NH_2), 3049 (stretching of C-H aromatic), 2944 (stretching of C-H aliphatic), 1651 (stretching of C=N), 1586 (stretching of C=C), 1232 (C-N) and 1163 (C-O). ^{1}H NMR (DMSO-d_6, δ in ppm) (**Fig. 1**): 5.33 (s, 1H, CH), 6.61 (s, 4H, -NH_2), 6.78-6.80 (d, 1H, Ar-H, *J*= 5.6 Hz), 6.93-6.94 (d, 1H, Ar-H, *J*= 5.6 Hz), 7.42-7.44 (d, 1H, Ar-H, *J*= 5.2 Hz), 10.95-11.28 (m, 4H, broad, hydroxy pyrimidine). ^{13}C NMR (100 MHz, (DMSO-d_6, δ in ppm) (**Fig. 2**): 30.98, 115.41, 128.27, 128.55, 137.86, 140.13, 143.76, 170.77.

2.5. P(P-T-A) synthesis by TMAPD polycondensation reaction in TPP/IL

The synthesis of P(P-T-A) was carried out from a compound containing multi polar thiophene, amine, and free hydroxyl chelating groups. It was particularly synthesized from a diamine-phenol compound in 1,3-dipropyl imidazolium bromide as an ionic liquid without using toxic triphenyl phosphite/N-methylpyrolidone/pyridine/LiCl that is needed in the common direct polycondensation. P(P-T-A) was synthesized by polycondensation of TMAPD using TPP-IL as catalyst and solvent by the following procedure: A flask of three-necked round-bottomed with the volume of 50 mL was fitted with a mechanical stirrer, a water cooled condenser, and argon gas, and then a mixture containing 1 mmol of TMAPD, 1 mmol of terephthalic acid, 0.7 g of 1,3-dipropyl imidazolium bromide {[1,3-$(pr)_2$im]Br} as IL, and 1.29 mmol of TPP was placed. The solution became sticky as the reaction continued at 110 °C for 2.5 h. In the following, the reaction mixture temperature was decreased to the RT, and the precipitation of P(P-T-A) was performed using 100 mL of methanol. After filtration, hot water was used for washing the precipitate. Afterward, the it was further refined in a Soxhlet apparatus using methanol for 24 h to eliminate the oligomers with low molecular weight. FT-IR (KBr, cm^{-1}): 3164-3337 (stretching

of O-H and NH_2), 3054 (stretching of C-H aromatic), 2958 (stretching of C-H aliphatic), 1683 (stretching of C=O amide), 1641 (stretching of C=N), 1593 (stretching of C=C), 1215 (C-N) and 1167 (C-O). ^{1}H NMR (DMSO-d_6, δ in ppm) (**Fig. 3**): 5.37 (s, 1H, CH), 7.25-7.27 (m, 2H, Ar-H), 7.44 (s, 1H, Ar-H), 7.99-8.00 (d, 2H, Ar-H, *J*= 3.2 Hz), 8.06-8.08 (d, 2H, Ar-H, *J*= 5.2 Hz), 11.01 (s, 1H, OH amide), 11.32 (m, 4H, broad, hydroxy pyrimidine).

2.6. Synthesis of CA-P(P-T-A)-NZFO magnetic nanocomposite

Sodium alginate powder was dissolved in DW with the concentration of 1.5 % (w/v) to prepare a sodium alginate solution. 0.5 g of P(P-T-A) and 0.7 g of $Ni_{0.2}Zn_{0.2}Fe_{2.6}O_4$ were fully dispersed in the sodium alginate solution with vigorous stirring for 24 h to achieve a homogeneous solution, A. Afterwards, solution A was added dropwise to the solution of $CaCl_2$ (0.05 M) and 2 % glutaraldehyde for gelation process, and then the mixture was mixed for 24 h. The desired product was collected by an external magnetic field, rinsed several times using DW until reaching the solution pH to 7, and dried at 50 °C. Finally, it was powdered.

2.7. Apparatuses

To analyze the morphology and chemical characterization of the products, FE-SEM and EDX were respectively applied using Zeiss Neon-40, Germany. 400 MHz and 100 MHz of Bruker Advance DRX instrument were respectively used to record ^{1}H NMR and ^{13}C NMR spectra by DMSO-d_6 as a solvent. FT-IR spectrophotometer (PerkinElmer, USA) was employed to identify the functional groups of the products. XRD (GBC MMA instrument) was used to characterize the crystallinity of the product in the range of 2θ = 10–70° at RT. To record the thermal decomposition properties of the products, a thermogravimetric analyzer (TGA) (Mettler TGA/SDTA 851e/LF/1100 thermobalance) under N_2 atmosphere at a rate of 10 °C/min was

applied. The magnetic properties of the products were studied by a vibrating sample magnetometer (VSM, Daghigh Kavir Corporation, Iran).

2.8. Adsorption experiments

The experiments related to batch ions adsorption using CA/P(P-T-A)/NZFO were performed by a laboratory shaker adjusted at 180 rpm. To explore the influence of solution pH, the pH values of metal ions solutions (30 mg/L) were adjusted from 1.5 to 5.5 using a pH meter.

Each solution containing 0.03 g of the adsorbent was shaken for 20 min at 25 ˚C. In order to perform kinetic experiments, the mixtures of 0.03 g of the nanocomposite and 50 mL of the solutions (REEs concentration: 30 mg/L) were agitated at various contact times (ranging from 2.5 to 70 min). For finding the adsorbent dosage influence on the adsorption process, various quantities of the nanocomposite in the range of 0.01-0.06 g were utilized by keeping the pH of the solutions at the optimized constant value. 0.04 g of the nanocomposite and the solutions at the concentrations ranging from 30 to 300 mg/L at RT were applied for isotherm study. The ionic strength of the solution was taken into consideration for its influence by the presence of $NaNO_3$ with the concentration in the range of 0.02-0.1 M. To assess the influence of temperature on the ions adsorption, the tests at various temperatures (25, 35, and 45 ˚C) were conducted. After the adsorption process, the nanocomposite was collected using an external magnet, and finally Agilent 4100 MP-AES Spectrometer was utilized to analyze the REEs concentration in the solutions. All the experiments were performed three times, and the experimental error was below 3 %. The average data were reported. The metal ions adsorption efficiency and the capacity of the ions adsorption by using CA/P(P-T-A)/NZFO were computed by the bellowing equations:

$$\text{Adsorption efficiency (\%)} = (C_0 - C_e)/C_o \times 100 \quad (1)$$

$q_e = (C_0 - C_e) \times V/m$ (2)

$q_t = (C_0 - C_t) \times V/m$ (3)

Where the parameters are as follows:

q_e (mg/g): the adsorbed ion quantity onto the nanocomposite at equilibrium, q_t (mg/g): the adsorbed ion quantity onto the nanocomposite at time t (min), C_0 (mg/L): the initial ion concentration, C_e (mg/L): the REEs concentration at equilibrium, C_t (mg/L): the REEs concentration at time t, V (L): the volume of solution, and m (g): the nanocomposite weight.

2.9. Batch reusability study

The reusability experiments were done by separating the nanocomposite loaded with the related ions from the solutions. In the following, DW was used to rinse the nanocomposite several times, and then it was contacted with 0.2 M HNO_3 (50 mL) for 2 h in order to desorb the ions. After separating the nanocomposite using an external magnet, the ions in the solutions were determined using Agilent 4100 MP-AES Spectrometer.

3. Results and discussion

3.1. Characterization of the synthesized products

The peaks in the NZFO XRD pattern detected at 2θ values ranging from 10° to 70° shown in **Fig. 4** correspond with JCPDS 08-0234 (nickel zinc ferrite standard pattern) [19]. For the estimation of the average size of the NZFO from the XRD pattern based on the Scherrer equation [20], its strongest reflection (2θ = 35.50°) was applied by considering its FWHM. The average size of NZFO particles was calculated to be 27.68 nm.

The morphology of the NZFO shown in **Fig. 5A** is homogenously spherical with a size of < 100 nm. As shown in **Fig. 5B**, the size of CA is micrometer, and NZFO and P(P-T-A) are

distributed on its surface or embedded. The results of FE-SEM images are a confirmation for the successful synthesis of the magnetic nanocomposite.

Fig. 6 indicates the EDX recorded for the analysis of the elements existing in the synthesized materials. The available peaks in **Fig. 6A** are zinc, nickel, iron, and oxygen that prove NZFO formation. The sulfur and calcium peaks along with the peaks of zinc, nickel, iron, and oxygen are shown in the EDX spectrum of the nanocomposite (**Fig. 6B**). It could be suggested the complete release of Na^{+} ions from sodium alginate matrix as a result of the crosslinking reaction of Na^{+}-alginate with Ca^{+2}.

The FT-IR spectra of CA, NZFO, P(P-T-A) and the nanocomposite are indicated in **Figs. 7A-7D**. The FT-IR spectrum of CA shows O-H stretching vibration at 3389 cm^{-1}. Besides, the asymmetrical stretching of carboxyl groups at 1622 cm^{-1}, the symmetrical stretching of carboxyl groups at 1423 cm^{-1}, and C-O-C stretching at 1052 cm^{-1} are characterized in the related figure [21]. For FT-IR of NZFO, the positions of the peaks are at 3424 and 1633 cm^{-1}, assigning to the stretching vibration of O-H [22]. The CTAB peaks are also detected as follows: anti-symmetric vibration of C-H at 2925 cm^{-1} and symmetric vibration of C-H at 2853 cm^{-1} [23]. In the related figure, two peaks are shown at 567 and 478 cm^{-1} that are assigned to the stretching vibrations of inherent metal at the tetrahedral site (Fe-O), and the stretching of octahedral metal (M-O), respectively [22]. The P(P-T-A) peaks are O-H and NH_2 stretching at 3164-3337 cm^{-1}, C-H aromatic stretching at 3054 cm^{-1}, C-H aliphatic stretching at 2958 cm^{-1}, C=O amide stretching at 1683 cm^{-1}, C=N stretching at 1641 cm^{-1}, C=C stretching at 1593 cm^{-1}, C-N at 1215 cm^{-1} and C-O at 1167 cm^{-1}. The FT-IR of the nanocomposite proves that its synthesis was done successfully by the observation of the peaks related to CA, P(P-T-A), and NZFO.

Fig. 8A presents the resulting P(P-T-A) thermo-stability. The curve of TGA indicates five steps for the P(P-T-A) weight loss. At the first step that is up to around 100 ˚C, 1.17 % weight loss is seen, attributing to the evaporation of water. From around 100 to 290 ˚C (second step), P(P-T-A) weight loss is 9.6 % because the aliphatic groups are degraded primarily. The range of 300 to 330 ˚C is the third step of weight loss for P(P-T-A), in which the polymers aromatic groups are gradually degraded, and their further decomposition leads to 44.16 % weight loss at the forth step. The polymer residue is completely degraded at the final step and converted to CO_2 and H_2O. The nanocomposite TGA curve is presented in **Fig. 8B**. As compared with P(P-T-A) TGA curve, an increase is observed in the thermal stability of the nanocomposite, meaning the shift of decomposition temperature to a higher temperature. This increase could be as a result of the inorganic presence in the composite, meaning that combining the composite with NZFO causes an increase in thermal stability.

The value of 45.87 emu/g obtained for the magnetic saturation of NZFO (**Fig. 9A**) indicates its superparamagnetic behavior. Combining NZFO with CA and P(P-T-A) causes that saturation magnetization decreases to 15.28 emu/g (**Fig. 9B**). In spite of this difference, using a magnetic field externally could easily separate the REEs-loaded nanocomposite from aqueous medium for the avoidance of secondary pollution (**Fig. 9C**).

3.2. Effect of pH

Solution initial pH value, as an essential parameter in the adsorption process, must be optimized to reach a favorable adsorption efficiency. In this research study, pH of the solutions was adjusted in the range of 1.5-5.5 to study the behavior of the REEs adsorption. The experiments at pH > 5.5 were not studied to avoid the REEs precipitation in the solutions. According to the results in **Fig. 10A**, the amounts of REEs adsorption at low pH values are low

because of the fact that the active sites of CA/P(P-T-A)/NZFO are protonated, causing the limitation of the available active sites for the ions adsorption. Amine groups are also partially protonated at low pH values. Consequently, electrostatic repulsion forces cause a limitation in the interaction between the protonated amine groups and metal ions. The active sites protonation decreases at higher pH values because of decreasing H^+ concentration, leading to higher adsorption efficiency [24]. Although the adsorption efficiencies of the ions at the pH of 4.5 are close to those obtained at pH of 5.5, pH of 5.5 was chosen for performing other parameters of adsorption process in order to reduce the acidity of the solution and perform the experiments in conditions closer to environmental or wastewater pH. According to the results, it should be also noted that CA/P(P-T-A)/NZFO is not selective towards an ion among Nd^{3+}, Tb^{3+}, and Dy^{3+}.

3.3. Effect of contact time

From the experimental data presented in **Fig. 10B**, the equilibrium state of the adsorption process occurs after approximately 50 min of contact time. At first, the rate of reaction is relatively fast, and the values of adsorption efficiencies in the first 2.5 min are 60.59 % (Nd^{+3}), 55.92 % (Tb^{+3}), and 57.31 % (Dy^{+3}), and then a lower rate is seen and eventually no more notable adsorption is obtained beyond 50 min for each ion. At the beginning of the process, the higher REEs adsorption efficiency is as a result of a large number of vacant functional groups of CA/P(P-T-A)/NZFO. In the continuation of the process, the formation of a monolayer by the adsorbed ions leads to exhaustion in the adsorbent capacity, and then the rate of metal ions transportation from the adsorbent exterior sites to its interior sites controls the uptake rate of the ions. It could be also noted that by considering the constant number of the active adsorption sites and the adsorption of only one ion by each active site in a monolayer, a rapid uptake of the ions by the adsorbent surface takes place initially. In the following, it decreases by intensifying the

competition of the ions in the solution for occupying and decreasing the available active sites [25].

3.4. Adsorption kinetics

To explore the kinetics of adsorption, the nonlinear models of intra-particle diffusion (IPD), pseudo-second-order (PSO), and pseudo-first-order (PFO) written in **Table 1** were utilized for fitting the REEs adsorption data [26,27]. The validity of each model was compared by Chi-square (χ^2) according to Eq. (4), since the coefficient of determination (R^2) may not be reasonable to select the best adsorption model in view of the fact that it only presents the fit between equations and experimental data, while the correlation between predicted and experimental values of the adsorption capacity is explained by χ^2. The lower values of χ^2 indicate a better fit.

$$\chi^2 = \sum_{i=1}^{n} \frac{(q_{e,exp} - q_{e,cal})^2}{q_{e,cal}} \quad (4)$$

Where the parameters are as follows:

n: data points number, $q_{e,exp}$: experimental adsorption capacity, and $q_{e,cal}$: computed adsorption capacity.

Table 1 presents the kinetic parameters acquired by modeling the experimental data (**Figs. S1-S3**). The values of R^2 obtained from fitting the data with PSO model are higher than the values acquired by PFO and IPD models. The χ^2 values acquired from PSO model (0.11–0.46) are lower in comparison with the values obtained from PFO (4.58–6.67) and IPD (3.81-5.52) models that strongly confirm PSO model as the best model to describe the REEs adsorption by CA/P(P-T-A)/NZFO. Furthermore, a comparison between the experimental equilibrium adsorption capacity ($q_{e,exp}$) and computed equilibrium adsorption capacity ($q_{e,cal}$) shows that the quantities given by PSO model are closer to the experimental data than those provided by PFO

and IPD models, describing the adsorption process by chemisorption mechanism. The equilibrium adsorption of Dy^{+3} (48.13 mg/g) is higher than that of Nd^{+3} (48.05 mg/g) and Tb^{+3} (47.43 mg/g). The initial sorption rate "h" has been extremely used to evaluate the rates of adsorption. In this study, the values of "h" for the REEs show that CA/P(P-T-A)/NZFO can adsorb Nd^{+3} (29.41 mg/g min) more rapidly than Dy^{+3} (27.68 mg/g min) and Tb^{+3} (26.05 mg/g min) from aqueous solution. It is also apparent from that the rate constant (K_2) of Nd^{+3} (0.01274 g/mg min) is higher than that of Dy^{+3} (0.01195 g/mg min) and Tb^{+3} (0.01158 g/mg min), indicating a higher affinity between Nd^{+3} ions and CA/P(P-T-A)/NZFO, which may be owing to the faster adsorption rate of Nd^{+3} compared with Dy^{+3} and Tb^{+3}. Based on IPD model, q_t versus $t^{0.5}$ should follow a linear plot that passes through the origin if it is the sole rate-limiting step [28]. As stated by the results, it may be deduced that IPD is not only the rate-limiting factor.

3.5. Effect of adsorbent dosage

One of the major factors that has a considerable influence on the ions adsorption is adsorbent dosage, determining the adsorbent potential via the number of biding sites that are accessible and active for the ions adsorption while the concentration is at constant value. The nanocomposite dosage effect on the adsorption efficiency of the REEs is illustrated in **Fig. 10C**. It is clear that the ability of the nanocomposite to adsorb the REEs enhances from 51.14 to 98.11 % for Nd^{+3}, 49.33 to 95.62 % for Tb^{+3}, and 50.66 to 98.15 % for Dy^{+3} by enhancing the dosage of adsorbent from 0.01 to 0.04 g. The increase in the ions adsorption by enhancing the adsorbent dosage is due to enhancement in the number of active sites and available surface area [29]. The state of equilibrium is obtained by means of the quantity of the nanocomposite required for maximum adsorption efficiency, and this is achieved by using 0.04 g of the adsorbent for the REEs. It is not remarkably changed by increasing the adsorbent dosage beyond 0.04 g.

3.6. Effect of concentration

The capacity of adsorption of CA/P(P-T-A)/NZFO was investigated by the influence of the initial REEs concentration. As presented in **Fig. 10D**, initial REEs concentration enhancement leads to a reduction in adsorption efficiency from 96.73 to 19.33 % for Nd^{+3}, 94.82 to 29.59 % Tb^{+3}, and 97.58 to 30.95 % for Dy^{+3}, while adsorption capacity at equilibrium for the REEs by the nanocomposite increases. By performing the experiments at 300 mg/L of the REEs, the capacity of adsorption obtained at 25 ◦C was respectively calculated to be 72.49 mg/g for Nd^{+3}, 110.95 mg/g for Tb^{+3}, and 116.05 mg/g for Dy^{+3}. When the REEs concentration is low in the solution, the ratio of surface area and the total available adsorption sites to the initial number of the ions in the solution is relatively high that leads the adsorption of the ions to be independent of the initial concentration of the ions; thus, the ions are easily adsorbed. By an increase in the REEs concentration, limitation in the total available adsorption sites results a reduction in the nanocomposite capacity towards the REEs adsorption [30]. The increase in adsorption capacity of the nanocomposite at higher initial concentration could be related to enhancement in mass transfer driving force that could overcome all the mass transfer resistances of the ions between the aqueous and solid phase, resulting in the higher probability of collision between the ions and adsorbent [31].

3.7. Adsorption isotherms

Langmuir and Freundlich in the form of nonlinear were utilized for fitting the adsorption data of the REEs. Langmuir model hypothesis is mentioned as follows: uniform and equivalent active sites on adsorbent surface, the adsorption process in a monomolecular layer, and no fundamental interaction between substances adsorbed on the surface of adsorbent. Freundlich

model hypothesizes a multilayer adsorption onto the heterogeneous surface of adsorbent. The models are written in **Table 2** [32,33].

The fitting of the isotherm data by the models are indicated in **Fig. S4**. The obtained values for the coefficient of determination (R^2) and parameters are presented in **Table 2**. According to the values of R_L, there are four cases that are mentioned as following: the process of adsorption with $R_L = 0$ is irreversible. It is linear if $R_L = 1$ while it is favorable if $0 < R_L < 1$. In contrast, it is unfavorable if $R_L > 1$ [34]. The values of R_L for the REEs are between 0 and 1, suggesting that the adsorption process of the REEs by the nanocomposite is favorable. The n values are > 1 (n_{Nd+3} = 9.85, n_{Tb+3} = 4.91, and n_{Dy+3} = 5.54), showing that the interaction between the nanocomposite and the REEs was strong. It is apparent from the obtained results that the Tb^{+3} and Dy^{+3} data are fitted well with Freundlich model, expressing a multilayer adsorption of these ions that takes place on a surface with non-uniform structure. In contrast, the best fit for Nd^{+3} adsorption data is obtained by Langmuir model according to the values of R^2 and χ^2, indicating that the adsorption of Nd^{+3} is monolayer adsorption. The value of the maximum monolayer adsorption capacity (q_m) of Nd^{+3} calculated by Langmuir model at 25 ˚C is 71.44 mg/g, which is close to the experimental data. **Table 3** compares the capacity of adsorption acquired by various adsorbents.

3.8. Effect of ionic strength

The efficiency of the REEs adsorption affected by ionic strength is indicated in **Fig. 11A**. The results show a significant effect of $NaNO_3$ on the REEs adsorption by the nanocomposite. When 0.02 M $NaNO_3$ is used, the adsorbent efficiency for the REEs decreases from 96.73 to 91.53 %, 94.82 to 88.83 %, and 97.58 to 93.3 % for Nd^{+3}, Tb^{+3}, and Dy^{+3}, respectively. By increasing $NaNO_3$ concentration from 0.02 to 0.1 M, a significant decrease in the ability of the

adsorbent to adsorb the ions is seen due to the competition of Na^{+} from the dissolution of $NaNO_3$ with the ions for interacting with the functional groups on the nanocomposite surface [58]. As for adsorption of Nd^{+3} and Tb^{+3}, $Nd^{+3} > Tb^{+3}$ can be seen for the order of adsorption efficiency at low concentration of $NaNO_3$, while it changes to $Tb^{+3} > Nd^{+3}$ at higher concentration of $NaNO_3$. This result suggests that ion exchange interaction could be a mechanism for the process of the REEs adsorption by the synthesized nanocomposite.

3.9. Temperature effect on the REEs adsorption

Different temperatures ranging from 25 to 45 ˚C were applied for the batch adsorption of the ions by the nanocomposite (0.04 g) at 90 mg/L of the ions and pH = 5.5. The results presented in **Table 4** show that raising temperature ranging from 25 to 45 ˚C results an increase in adsorption efficiency of the nanocomposite from 61.71 to 69.15 % for Nd^{+3}, 66.79 to 77.25 % for Tb^{+3}, and 69.33 to 79.73 % for Dy^{+3}. An enhancement in adsorption efficiency is mostly as a result of the surface activity increase that proposes an endothermic adsorption process between the REEs and nanocomposite.

3.10. Thermodynamic parameters evaluation

Gibbs free energy (ΔG°, kJ/mol), enthalpy (ΔH°, kJ/mol), and entropy (ΔS°, kJ/mol K), as the parameters of thermodynamic, were computed using the equations as following [59]:

$$K_d = q_e/C_e \quad (5)$$

$$\text{Ln } K_d = \Delta S^{\circ}/R - \Delta H^{\circ}/RT \quad (6)$$

$$\Delta G^{\circ} = - RT \text{ Ln } K_d \quad (7)$$

Where the parameters are as follows: K_d: the coefficient of distribution, C_e (mg/L): the concentration of the REEs in the solution at equilibrium, T: the temperature (K), and R: the gas

constant (8.314 J/mol K). Based on the plot of Ln K_d versus 1/T (**Fig. 11B**), the computed values of ΔH° (from the slop) and ΔS° (from the intercept) are presented in **Table 4**.

The value of ΔG° is negative and small that increases by increasing temperature, which indicates a reduction in Gibbs energy in the adsorption process. The ΔG° negative values demonstrate that the process is naturally spontaneous and feasible. The positive ΔH° values confirm the nature of adsorption to be endothermic, and the values of $\Delta S^\circ > 0$ describe that at the interface of nanocomposite-solution, randomness increases during the process of REEs adsorption [56]. According to the obtained parameters of thermodynamic, the possibility of applying CA/P(P-T-A)/NZFO for the REEs adsorption is confirmed.

3.11. Reusability studies

The regeneration of an adsorbent is important in designing a process of adsorption. To explore the reusability of the nanocomposite, desorption test was performed by using HNO_3 solution with the concentration of 0.2 M. Firstly, the nanocomposite was loaded with 30 mg/L solutions of the REEs. The concentration of each metal was determined by the ICP after the separation of the loaded adsorbent with an external magnet. The loaded nanocomposite was completely rinsed using DW to wash the unadsorbed ions and then dried at 40 ˚C. Secondly, 50 mL of HNO_3 solution at RT was used for 2 h of desorption process at 180 rpm of a shaker. After finishing the process, each metal concentration was calculated. Four adsorption-desorption cycles were performed to test the nanocomposite reusability. Desorption efficiencies were obtained to be > 89 % (Nd^{+3}), 91 % (Tb^{+3}), and 95 % (Dy^{+3}). As illustrated in **Fig. 11C**, after the fourth cycle, the adsorption performance declines from 96.12 to 91.78 % for Nd^{+3}, 93.91 to 90.36 % for Tb^{+3}, and 96.85 to 93.56 % for Dy^{+3}. The results represent an efficient regeneration of the nanocomposite by HNO_3 solution with the concentration of 0.2 M and reutilization with an

insignificant decline in its adsorption efficiency that could confirm the economy of the adsorption process. The reasons for the decrease in adsorption efficiency after the forth cycle might be due to the chemically bonding of the ions with the functional groups that cannot be desorbed easily, decrease in the functional groups during acid treatment, and a few decrease in the dosage of adsorbent during cycles. Nevertheless, the obtained results reveal that the adsorbents can be potentially used for the adsorption of the REEs.

3.12. REEs competitive adsorption

The synthesized nanocomposite with the dosage of 0.04 g was applied in a ternary solution of the REEs with the ratio of 1:1:1 (30 mg/L of each ion) for evaluating the competitive adsorption of the REEs. In a multi-component system, antagonism, synergism, and non-interaction effects take place depending on the value of q_{mix}/q_0 [60]. The q_{mix}/q_0 values were 0.23 (Nd^{+3}), 0.51 (Tb^{+3}), and 0.51 (Dy^{+3}). The values of q_{mix}/q_0 are < 1, indicating antagonism effect of each ion on the adsorption of other REEs. Adsorption efficiency reduction was seen with the values of 22.3 % (Nd^{+3}), 48.05 % (Tb^{+3}), and 50.28 % (Dy^{+3}). The EDX spectrum (**Fig. 12**) recorded after the REEs adsorption process shows the related peaks of the REEs, which prove their successful adsorption by the synthesized nanocomposite.

4. Conclusion

In this study, CA/P(P-T-A)/NZFO magnetic nanocomposite was synthesized and characterized using various methods including XRD, FE-SEM, EDX, NMR, TGA, VSM, and FT-IR. The synthesized nanocomposite adsorption efficiency was investigated by conducting comprehensive experiments in aqueous solutions for the REEs adsorption. The optimum conditions for maximum adsorption efficiency were pH = 5.5 and 0.04 g of the nanocomposite in the solutions containing the REEs at the concentration of 30 mg/L. The REEs adsorption kinetic

onto the nanocomposite was well explained by PSO in comparison with PFO and IPD models. In addition, the equilibrium adsorption data were tested by using the nonlinear models of Freundlich and Langmuir. A well description of the adsorption data of Tb^{+3} and Dy^{+3} was obtained by Freunlich model. As for the adsorption of Nd^{+3}, Langmuir was found to be a suitable model for fitting the adsorption data, and 71.44 mg/g was the maximum capacity for Nd^{+3} adsorption. The calculated parameters of ΔH°, ΔG°, and ΔS° showed that the adsorption of the REEs was endothermic. An eluent of HNO_3 (0.2 M) was used for the desorption of the REEs, and the results of adsorption-desorption cycles indicated that the nanocomposite adsorption efficiency decreased from 96.12 to 91.78 % for Nd^{+3}, 93.91 to 90.36 % for Tb^{+3}, and 96.85 to 93.56 % for Dy^{+3} after the forth cycle.

Credit author statement

Hamedreza Javadian: Investigation, Acquisition of data, Analysis and/or interpretation of data, Drafting the manuscript and Revising the manuscript. **Montserrat Ruiz**: Acquisition of data and Supervision. **Mehdi Taghavi**: Experimental, Acquisition of data, Analysis and/or interpretation of data. **Ana Maria Sastre**: Conceptualization and supervision.

Declaration of interests

This work has been supported by the Spanish Ministry of Economy and Competitiveness (Ref. CTM2017-83581-R). Hamedreza Javadian acknowledges the financial support received (Ref. BES-2015-072506).

Acknowledgments

This work has been supported by the Spanish Ministry of Economy and Competitiveness (Ref. CTM2017-83581-R). Hamedreza Javadian acknowledges the financial support received (Ref. BES-2015-072506).

References

[1] Z. Zhao, X. Sun, Y. Dong, Synergistic Effect of doped functionalized ionic liquids in silica hybrid material for rare earth adsorption, Ind. Eng. Chem. Res. 55 (2016) 2221−2229.

[2] W. Bonificio, D.R. Clarke, Rare-earth separation using bacteria, Environ. Sci. Technol. Lett. 3 (2016) 180-184.

[3] C. Li, Z. Zhuang, F. Huang, Z. Wu, Y. Hong, Z. Lin, Recycling rare earth elements from industrial wastewater with flowerlike nano-$Mg(OH)_2$, ACS Applied Materials & Interfaces 5 (19) (2013) 9719-25.

[4] European Commission, 2010, Critical raw materials for the EU. Report of the ad-hoc Working Group on defining critical raw materials. http://ec.europa.eu/enterprise/policies/rawmaterials/files/docs/report-b_en.pdf (accessed 17.01.17).

[5] C. Tunsu, M. Petranikova, M. Gergorić, C. Ekberg, T. Retegan, Reclaiming rare earth elements from end-of-life products: A review of the perspectives for urban mining using hydrometallurgical unit operations, Hydrometallurgy 156 (2015) 239-258.

[6] M. Wang, X. Li, W. Hua, L. Shen, X. Yu, X. Wang, Electrospun poly(acrylic acid)/silica hydrogel nanofibers scaffold for highly efficient adsorption of lanthanide ions and its photoluminescence performance, ACS Appl. Mater. Interfaces. 8 (2016) 23995-24007.

[7] A.A. Zaki, T. El-Zakla, M.A.E. Geleel, Modeling kinetics and thermodynamics of Cs^{+} and Eu^{3+} removal from waste solutions using modified cellulose acetate membranes. J. Membr. Sci. 401-402 (2012) 1-12.

[8] Y. Zhu, Y. Zheng, A. Wang, A simple approach to fabricate granular adsorbent for adsorption of rare elements. Int. J. Biol. Macromol. 72 (2015) 410-420.

[9] F. Zhao, E. Repo, Y. Meng, X. Wang, D. Yin, M. Sillanpaa, An EDTA-β-cyclodextrin material for the adsorption of rare earth elements and its application in preconcentration of rare earth elements in seawater. J. Colloid Interface Sci. 2016, 465, 215-224.

[10] H. Ren, Z. Gao, D. Wu, J. Jiang, Y. Sun, C. Luo, Efficient Pb(II) removal using sodium alginate–carboxymethylcellulose gel beads: Preparation, characterization, and adsorption mechanism, Carbohydr. Polym. 137 (2016) 402–409.

[11] N.M. Mahmoodi, Magnetic ferrite nanoparticle–alginate composite: Synthesis, characterization and binary system dye removal, J. Taiwan Inst. Chem. Eng. 44 (2013) 322–330.

[12] J.A. Reglero Ruiz, M. Trigo-López, F.C. García, J.M. García, Functional aromatic polyamides, Polymers 9(9) 2017 414.

[13] K. Marchildon, Polyamides – Still strong after seventy years, Macromol. React. Eng. 5 (2011) 22-54.

[14] M. Ghaemy, B. Aghakhani, M. Taghavi, S.M. AminiNasab, M. Mohseni, Synthesis and characterization of new imidazole and fluorene–bisphenol based polyamides: Thermal, photophysical and antibacterial properties, React. Funct. Polym. 73 (2013) 555-563.

[15] D. Mecerreyes, Applications of ionic liquids in polymer science and technology. Springer, 2015.

[16] J. Lu, F. Yan, J. Texter, Advanced applications of ionic liquids in polymer science, Prog. Polym. Sci. 34 (2009) 431-448.

[17] E.I. Lozinskaya, A.S. Shaplov, M.V. Kotseruba, L.I. Komarova, K.A. Lyssenko, M.Y. Antipin, D.G. Golovanov, Y.S. Vygodskii, "One- pot" synthesis of aromatic poly(1,3,4-oxadiazole)s in novel solvents—ionic liquids. J Polym Sci Pol Chem 44 (2006) 380–394.

[18] Y.S. Vygodskii, E.I. Lozinskaya, A.S. Shaplov, K.A. Lyssenko, M.Y. Antipin, Y.G. Urman, Implementation of ionic liquids as activating media for polycondensation processes, Polymer 45 (2004) 5031–5045.

[19] D. Ni, Z. Lin, P. Xiaoling, W. Xinqing, G. Hongliang, Preparation and characterization of nickel-zinc ferrites by a solvothermal method, Rare Metal Mat Eng. 44(9) (2015) 2126-2131.

[20] K. Nejati, R. Zabihi, Preparation and magnetic properties of nano size nickel ferrite particles using hydrothermal method, Chem. Cent. J. 6 (2012) 23.

[21] R. Fabryanty, C. Valencia, F. Edi Soetaredjo, J. Nyoo Putro, S. Permatasari Santoso, A. Kurniawan, Y.H. Ju, S. Ismadji, Removal of crystal violet dye by adsorption using bentonite-alginate composite, J. Environ. Chem. Eng. 5 (2017) 5677-5687.

[22] A.S.A. Bakr, Y.M. Moustafa, E.A. Motawea, M.M. Yehia, M.M.H. Khalil, Removal of ferrous ions from their aqueous solutions onto $NiFe_2O_4$–alginate composite beads, J. Environ. Chem. Eng. 3 (2015) 1486–1496.

[23] S.A. Elfeky, S. Ebrahim Mahmoud, A. Fahmy Youssef, Applications of CTAB modified magnetic nanoparticles for removal of chromium (VI) from contaminated water, J. Adv. Res. 8(4) (2017) 435–443.

[24] Y. Song, L.Y. Yang, Y. Wang, D. Yu, J. Shen, X. Ouyang, Highly efficient adsorption of Pb(II) from aqueous solution using amino-functionalized SBA-15/calcium alginate microspheres as adsorbent, Int. J. Biol. Macromol. 125 (2019) 808-819.

[25] P. Chakravarty, N.S. Sarma, H.P. Sharma, Removal of Pb (II) from aqueous solution using heartwood of Areca catechu powder, Desalination 256 (2010) 16–21.

[26] H. Javadian, M. Torabi Angaji, M. Naushad, Synthesis and characterization of polyaniline/γ-alumina nanocomposite: A comparative study for the adsorption of three different anionic dyes, J. Ind. Eng. Chem. 20 (2014) 3890-3900.

[27] H. Javadian, P. Vahedian, M. Toosi, Adsorption characteristics of Ni(II) from aqueous solution and industrial wastewater onto Polyaniline/HMS nanocomposite powder, Appl. Surf. Sci. 284 (2013) 13-22.

[28] M.L.F.A. De Castro, M.L.B. Abad, D.A.G. Sumalinog, R.R.M. Abarca, P. Paoprasert, M.D.G. de Luna, Adsorption of methylene blue dye and Cu(II) ions on EDTA-modified bentonite: Isotherm, kinetic and thermodynamic studies, Sustain. Environ. Res. 28 (2018) 197-205.

[29] Z.H. Hua, A. Mohamed Omer, X. Ouyang, D. Yu, Fabrication of carboxylated cellulose nanocrystal/sodium alginate hydrogel beads for adsorption of Pb(II) from aqueous solution, Int. J. Biol. Macromol. 108 (2018) 149–157.

[30] G. Zhou, Y. Wang, R. Zhou, C. Wang, Y. Jin, J. Qiu, C. Hua, Y. Cao, Synthesis of amino-functionalized bentonite/$CoFe_2O_4$@MnO_2 magnetic recoverable nanoparticles for aqueous Cd^{2+} removal, Sci. Total Environ. 682 (2019) 505-513.

[31] Ramya Prasanthi Mokkapati, Venkata Nadh Ratnakaram, and Jayasravanthi Mokkapati Mass transfer, kinetic, equilibrium, and thermodynamic study on removal of divalent lead from

aqueous solutions using agrowaste biomaterials, *Musa acuminata*, *Casuarina equisetifolia* L., and *Sorghum bicolor*, Theor. Found. Chem. Eng. 53 (2019) 578–590.

[32] H. Javadian, F. Ghorbani, H. Tayebi, S.M. Hosseini Asl, Study of the adsorption of Cd (II) from aqueous solution using zeolite-based geopolymer, synthesized from coal fly ash; kinetic, isotherm and thermodynamic studies, Arab. J. Chem. 8 (2015) 837-849.

[33] H. Javadian, M. Ghasemi, M. Ruiz, A.M. Sastre, S.M. Hosseini Asl, M. Masomi, Fuzzy logic modeling of Pb (II) sorption onto mesoporous NiO/$ZnCl_2$-*Rosa Canina-L* seeds activated carbon nanocomposite prepared by ultrasound-assisted co-precipitation technique, Ultrason. Sonochem. 40 (2018) 748-762.

[34] H. Javadian, M. Taghavi, Application of novel Polypyrrole/thiol-functionalized zeolite Beta/MCM-41 type mesoporous silica nanocomposite for adsorption of Hg^{2+} from aqueous solution and industrial wastewater: Kinetic, isotherm and thermodynamic studies, Appl. Surf. Sci. 289 (2014) 487–494.

[35] E. Liu, X. Zheng, X. Xu, F. Zhang, E. Liu, Y. Wang, C. Li, Y. Yan, Preparation of diethylenetriamine-modified magnetic chitosan nanoparticles for adsorption of rare-earth metal ions, New J. Chem. 41 (2017) 7739-7750.

[36] J. Roosen, K. Binnemans, Adsorption and chromatographic separation of rare earths with EDTA- and DTPAfunctionalized chitosan biopolymers. J Mater Chem A. 2 (2014) 1530–1540.

[37] I.V. Melnyk, V.P. Goncharyk, L.I. Kozhara, G.R. Yurchenko, A.K. Matkovsky, Y.L. Zub, B. Alonso, Sorption properties of porous spray-dried microspheres functionalized by phosphonic acid groups, Microporous Mesoporous Mater. 153 (2012) 171–177.

[38] T. Kegl, I. Ban, A. Lobnik, A. Košak, Synthesis and characterization of novel γ-Fe_2O_3-$NH_4OH@SiO_2$(APTMS) nanoparticles for dysprosium adsorption, J. Hazard. Mater. 378 (2019) 120764.

[39] A. Negrea, A. Gabor, C.M. Davidescu, M. Ciopec, P. Negrea, N. Duteanu, A. Barbulescu, Rare earth elements removal from water using natural polymers, Sci Rep. 8 (2018) 316.

[40] Y.R. Lee, K. Yu, S. Ravi, W.S. Ahn, Selective adsorption of rare earth elements over functionalized Cr-MIL-101. Appl Mater Interfaces. 10 (2018) 23918-23927.

[41] X-H. Qi, K-Z Du, M-L Feng, Y-J Gao, X-Y. Huang, M.G. Kanatzidis, Layered $A_2Sn_3S_7 \cdot 1.25H_2O$ (*A* = organic cation) as efficient ion-exchanger for rare earth element recovery, J. Am. Chem. Soc. 2017, 139, 12, 4314-4317.

[42] S.M.A. Koochaki-Mohammadpour, M. Torab-Mostaedi, A. Talebizadeh-Rafsanjani, F. Naderi-Behdani, Adsorption isotherm, kinetic, thermodynamic, and desorption studies of lanthanum and dysprosium on oxidized multiwalled carbon nanotubes. J Dispers Sci Technol 35 (2014) 244–254.

[43] M.M. Yusoff, N.R. Nik Mostapa, Md. Shaheen Sarkar, T.K. Biswas, Md. Lutfor Rahman, S.E. Arshad, M.S. Sarjadi, A.D. Kulkarni, Synthesis of ion imprinted polymers for selective recognition and separation of rare earth metals, J. Rare Earth 35 (2017) 177-186.

[44] H.A. Madbouly, N.E. El-Hefny, Y.A. El-Nadi, Adsorption and separation of terbium(III) and gadolinium(III) from aqueous nitrate medium using solid extractant, Sep Sci Technol. (2019) 1-13.

[45] S. Tong, S. Zhao, W. Zhou, R. Li, Q. Jia, Modification of multi-walled carbon nanotubes with tannic acid for the adsorption of La, Tb and Lu ions, Microchim Acta 174 (2011) 257–264.

[46] D. Baybaş, U. Ulusoy, Polyacrylamide–clinoptilolite/Y-zeolite composites: Characterization and adsorptive features for terbium, J Hazard Mater 187(1) (2011) 241–249.

[47] R. Akkaya, Synthesis and characterization of a new low-cost composite for the adsorption of rare earth ions from aqueous solutions, Chem Eng J 200 (2012) 186–191.

[48] R. Akkaya, Terbium adsorption onto polyhydroxyethylmethacrylate–hydroxyapatite composite and its modified composition by phytic acid, Desalin Water Treat 52 (2014) 1440-1447.

[49] F.A. Alakhras, K.A. Dari, M.S. Mubarak, Synthesis and chelating properties of some Poly (Amidoxime-hydroxamic Acid) resins toward some trivalent lanthanide metal ions, J Appl Polym Sci 97(2) (2005) 691–696.

[50] M.A. Attia, S.I. Moussa, R.R. Sheha, H.H. Someda, E.A. Saad, Hydroxyapatite/$NiFe_2O_4$ superparamagnetic composite: Facile synthesis and adsorption of rare elements, Appl. Radiat. Isot. 145 (2019) 85-94.

[51] N.S. Reddy, K.M. Rao, S.V. Krishna, C.S. Ha, Synthesis of 1–acryloyl–3–phenyl thiourea based pH sensitive hydrogels for removal of samarium and terbium. Macromol. Res. 24 (2016) 494–501.

[52] M.R. Awual, N.H. Alharthi, Y. Okamoto, M.R. Karim, M.E. Halim, M.M. Hasan, M.M. Rahman, M.M. Islam, M.A. Khaleque, M.C. Sheikh, Ligand field effect for Dysprosium(III) and Lutetium(III) adsorption and EXAFS coordination with novel composite nanomaterials, Chem. Eng. J. 320 (2017) 427-435.

[53] R.M. Ashour, R. El-Sayed, A.F. Abdel-Magied, A.A. Abdel-Khalek, M.M. Ali, K. Forsberg, A. Uheida, M. Muhammed, J. Dutta, Selective separation of rare earth ions from

aqueous solution using functionalized magnetite nanoparticles: kinetic and thermodynamic studies, Chem. Eng. J. 327 (2017) 286–296.

[54] H. Aghayan, A. Mahjoub, A. Khanchi, Samarium and dysprosium removal using 11-molybdo-vanadophosphoric acid supported on Zr modified mesoporous silica SBA-15, Chem. Eng. J. 225 (2013) 509–519.

[55] T. Kaneko, F. Nagata, S. Kugimiya, K. Katob, Optimization of carboxyl-functionalized mesoporous silica for the selective adsorption of dysprosium, J Environmen Chem Eng 6 (2018) 5990-5998.

[56] X. Zheng, Y. Zhang, T. Bian, Y. Zhang, Z. Li, J. Pan, Oxidized carbon materials cooperative construct ionic imprinted cellulose nanocrystals films for efficient adsorption of Dy(III), Chem Eng J 381 (2020) 122669.

[57] X. Zheng, E. Liu, F. Zhang, Y. Yan, J. Pan, Efficient adsorption and separation of dysprosium from NdFeB magnets in an acidic system by ion imprinted mesoporous silica sealed in a dialysis bag, Green Chem. 18 (2016) 5031–5040.

[58] K. Srinivasa Rao, G. Roy Chaudhury, B.K. Mishra, Kinetics and equilibrium studies for the removal of cadmium ions from aqueous solutions using Duolite ES 467 resin, Int. J. Miner. Process. 97 (2010) 68–73.

[59] S. He, C. Han, H. Wang, W. Zhu, S. He, D. He, Y. Luo, Uptake of arsenic(V) using alumina functionalized highly ordered mesoporous SBA-15 (Alx-SBA-15) as an effective adsorbent, J. Chem. Eng. Data. 60 (2015) 1300-1310.

[60] F. Wang, Y. Pan, P. Cai, T. Guo, H. Xiao, Single and binary adsorption of heavy metal ions from aqueous solutions using sugarcane cellulose-based adsorbent, Bioresour Technol. 241 (2017) 482–490.

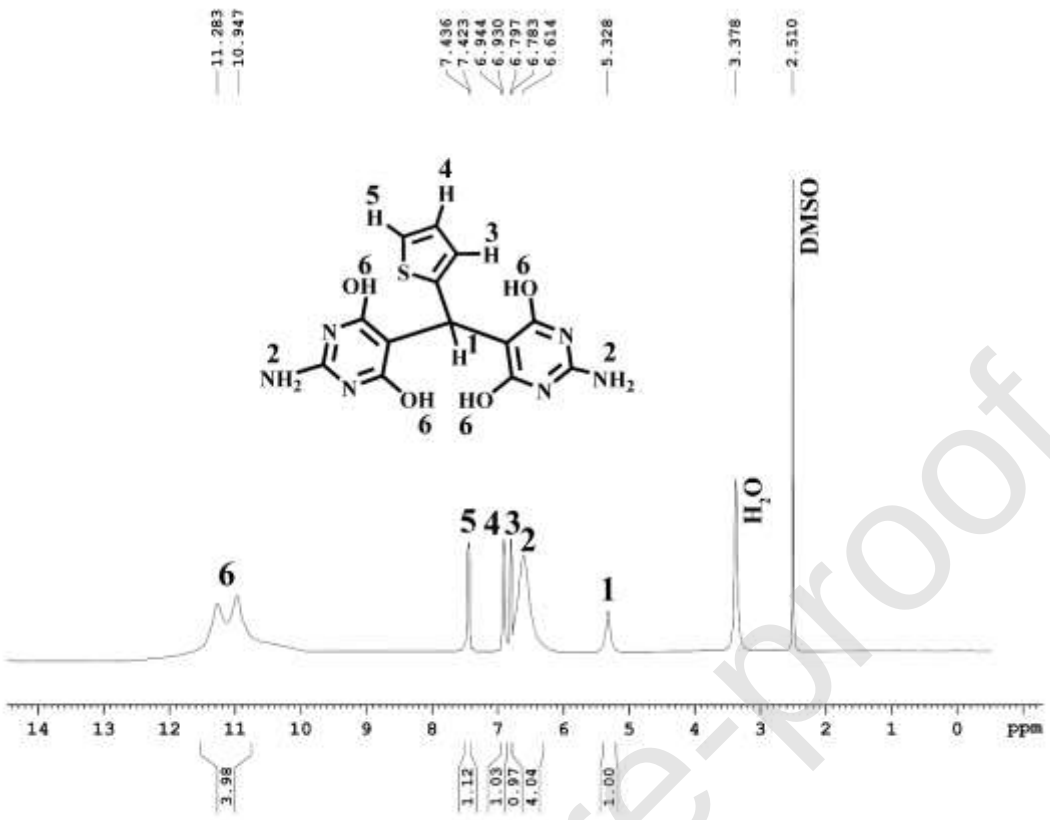

Fig. 1. The monomer ^{1}H NMR.

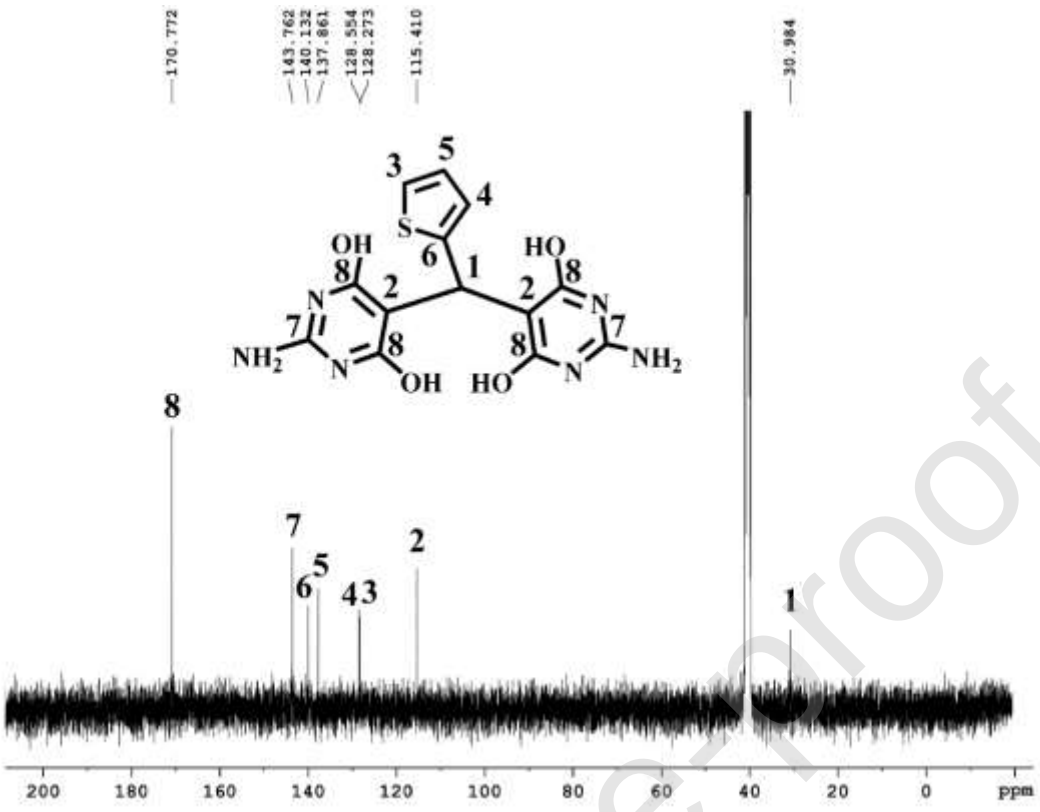

Fig. 2. The monomer ^{13}C NMR.

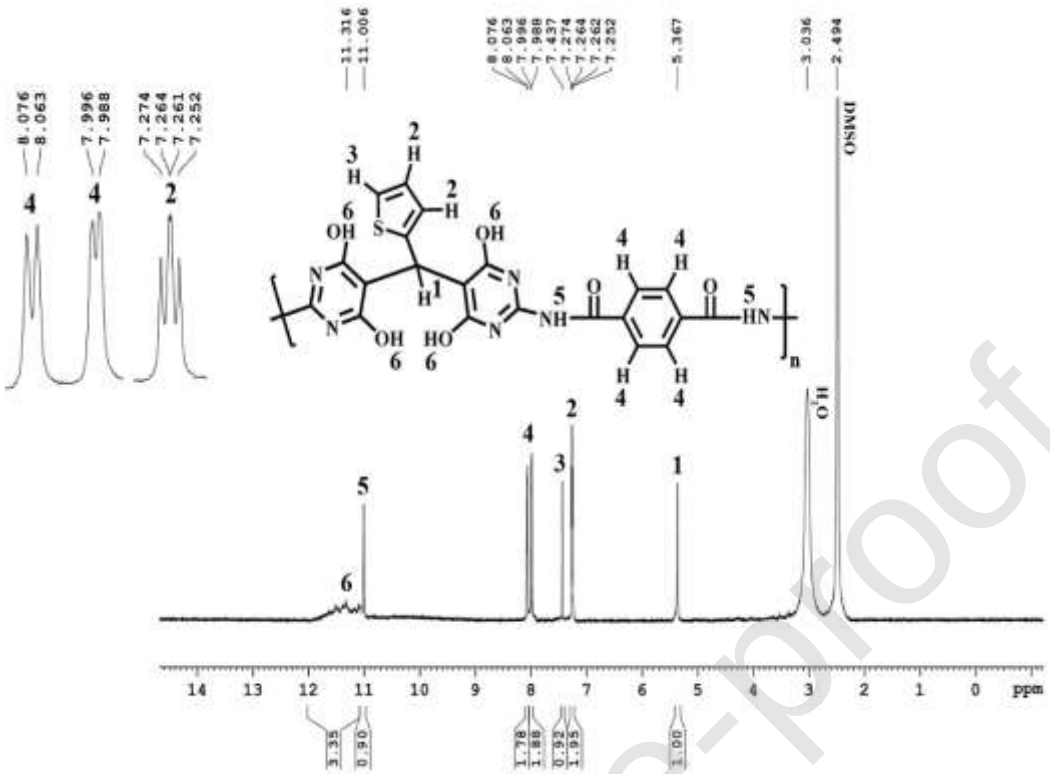

Fig. 3. P(P-T-A) ^{1}H NMR.

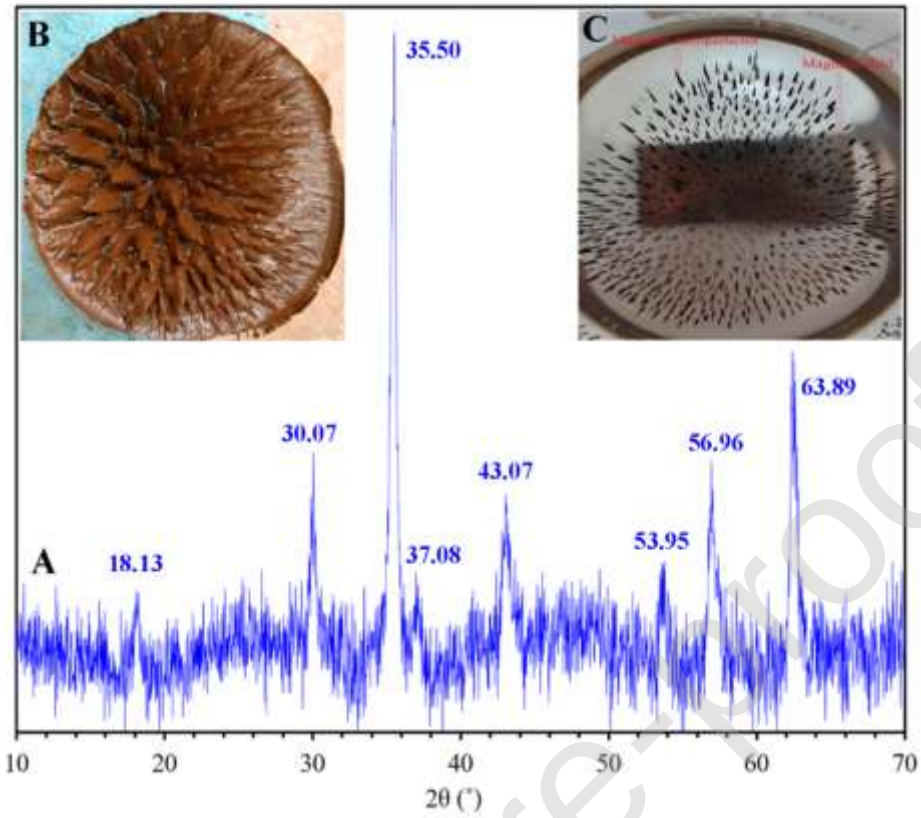

Fig. 4. (A) NZFO XRD pattern; NZFO photograph (B) prior to drying and (C) after drying under an external magnetic field.

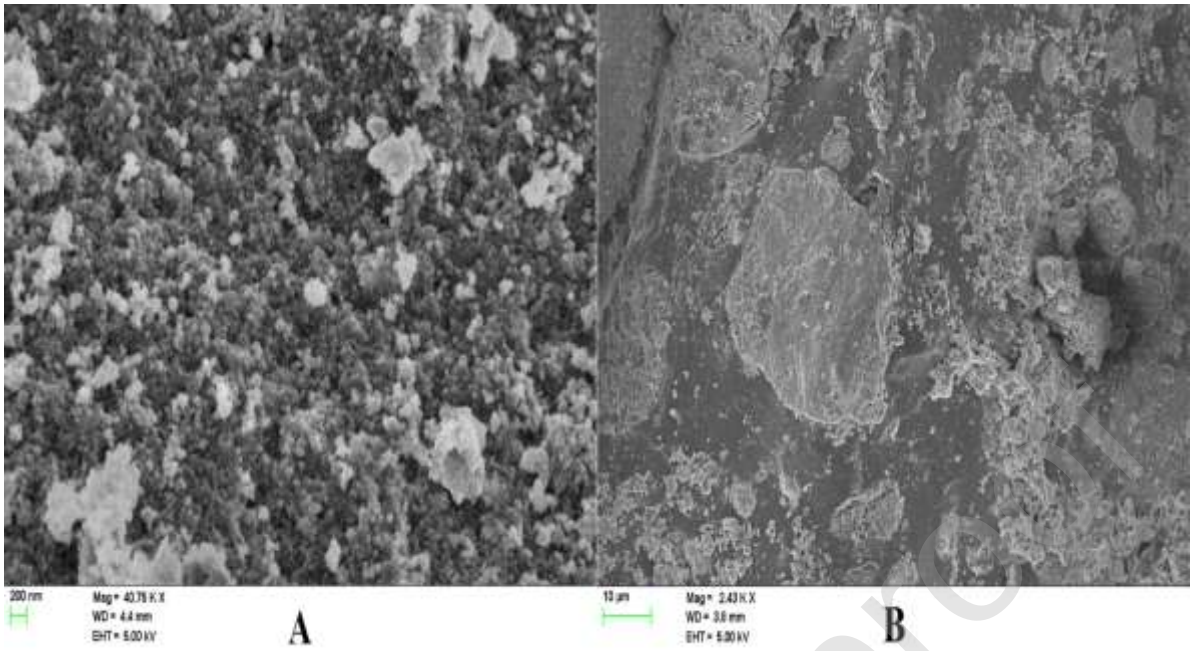

Fig. 5. Image of FE-SEM for (A) NZFO and (B) CA-P(P-T-A)-NZFO.

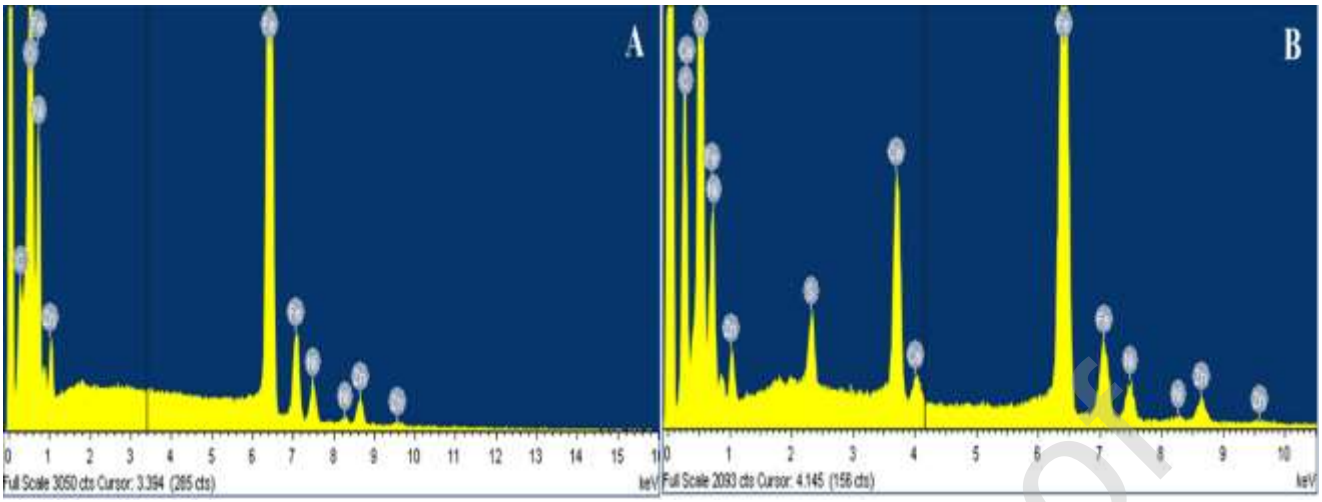

Fig. 6. Spectrum of EDX for (A) NZFO and (B) CA-P(P-T-A)-NZFO.

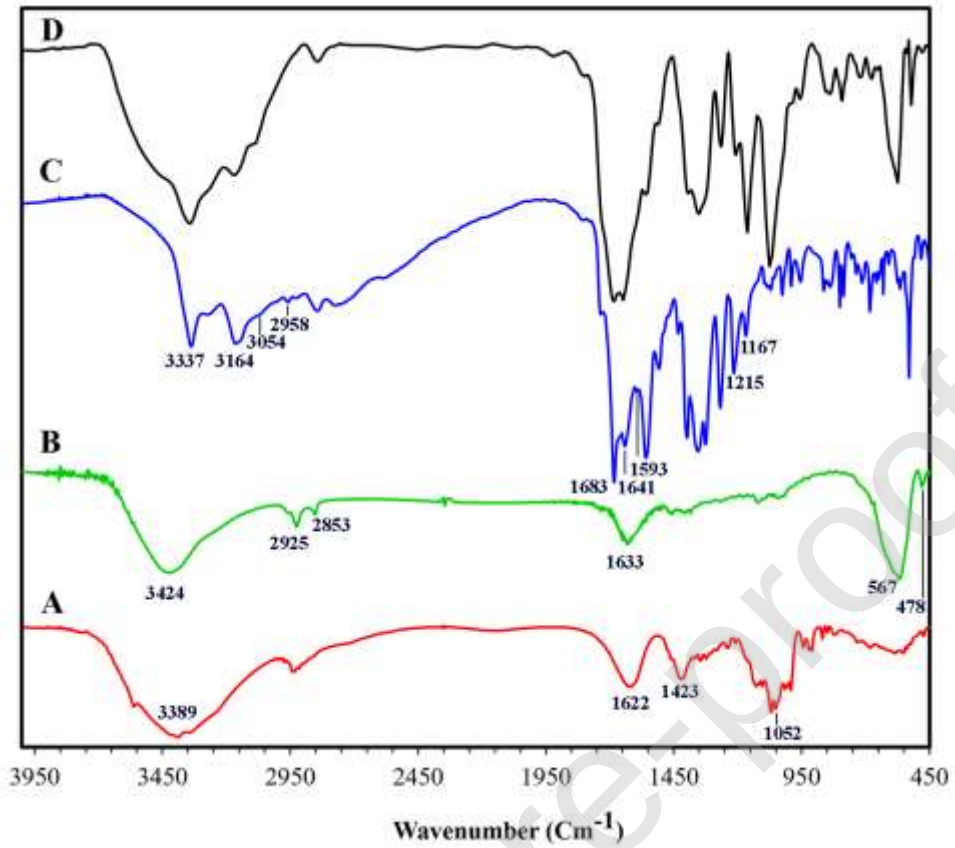

Fig. 7. Spectrum of FT-IR for (A) CA, (B) NZFO, (C) P(P-T-A), and (D) CA-P(P-T-A)-NZFO.

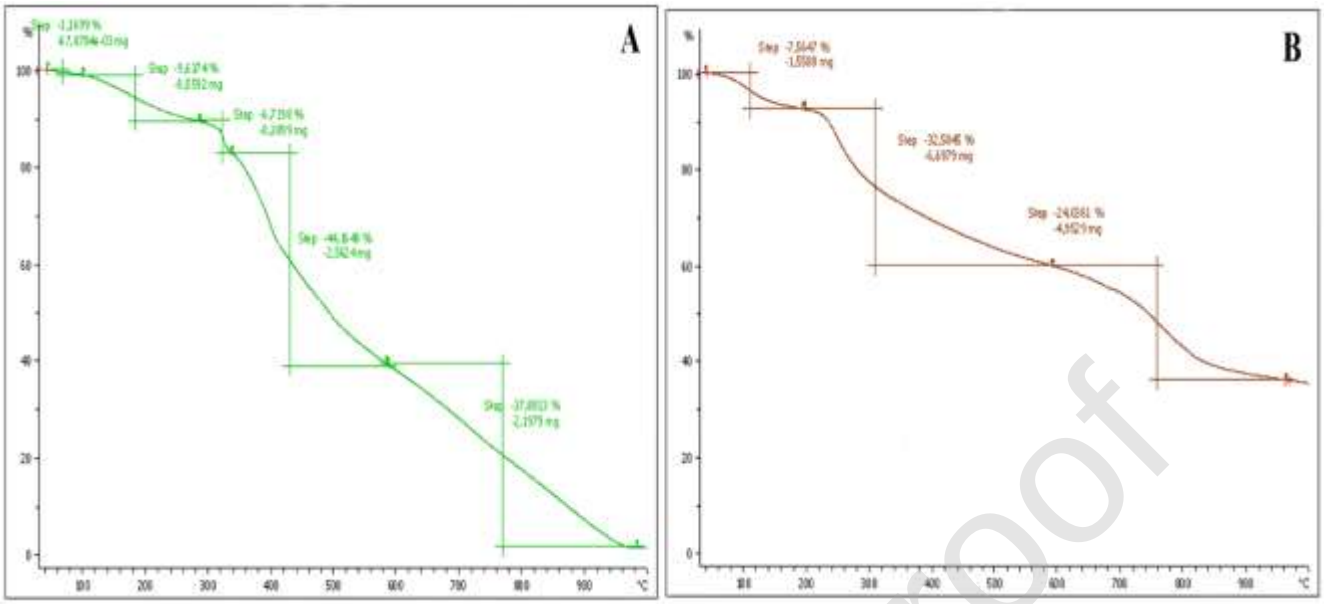

Fig. 8. Curve of TGA for (A) P(P-T-A) and (B) CA-P(P-T-A)-NZFO.

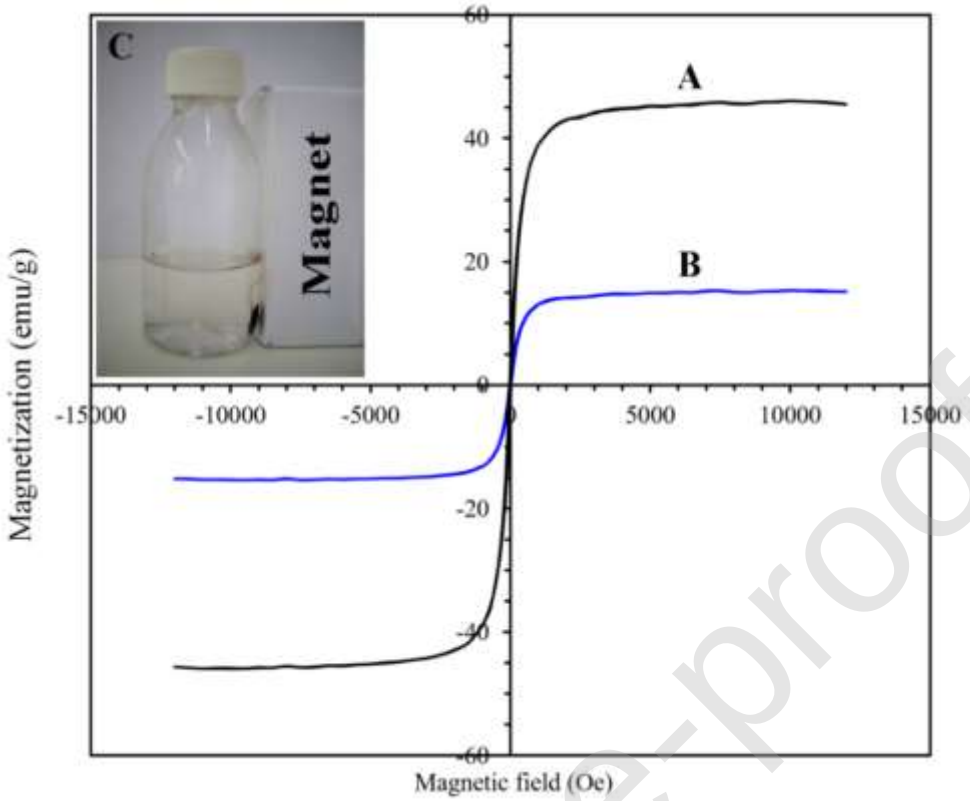

Fig. 9. Curve of magnetization for (A) NZFO and (B) CA-P(P-T-A)-NZFO; (C) Separation of the REEs-loaded nanocomposite by an external magnetic field.

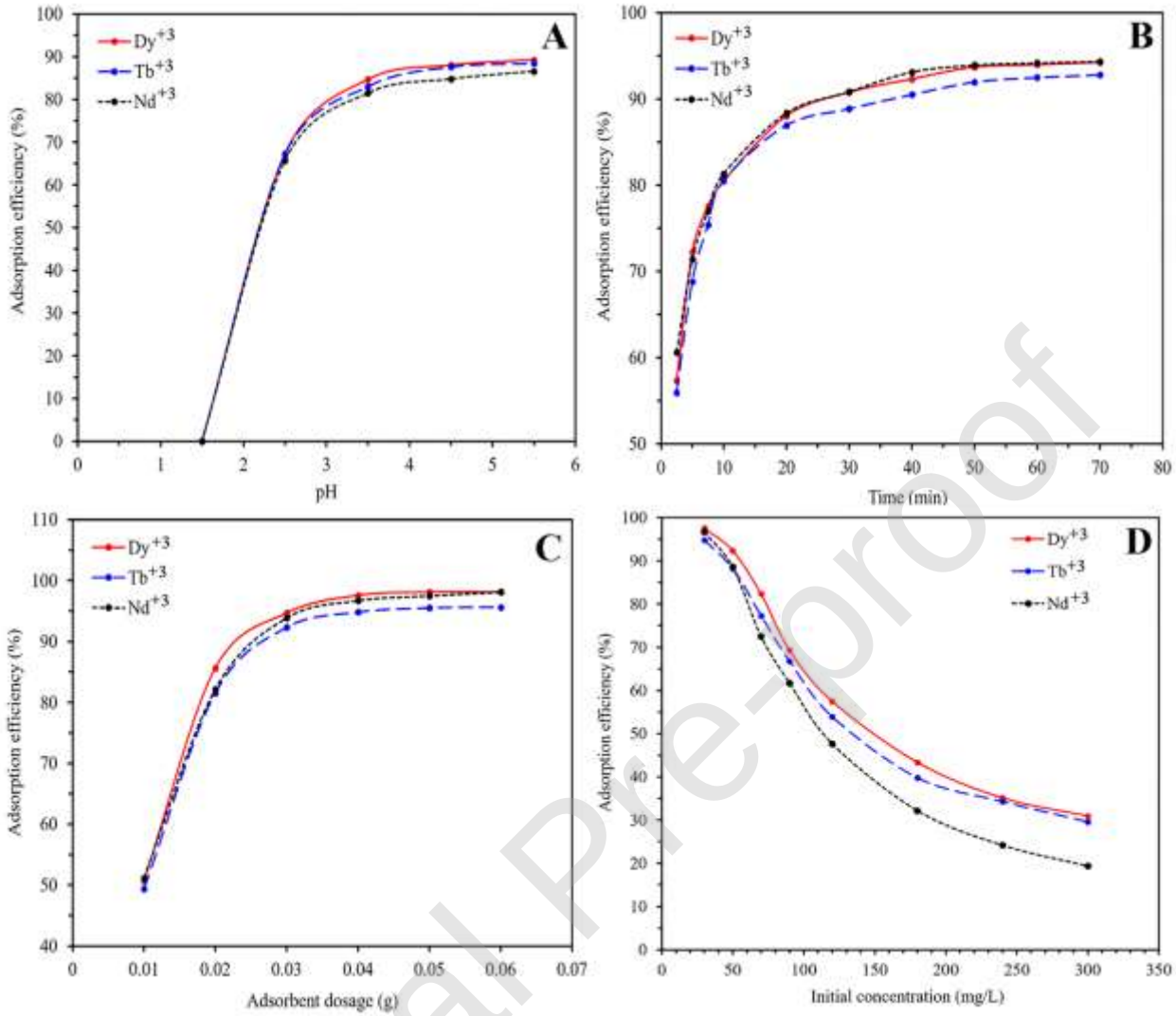

Fig. 10. (A) pH effect, (B) contact time effect, (C) adsorbent dosage effect, and (D) initial concentration effect on the REEs adsorption.

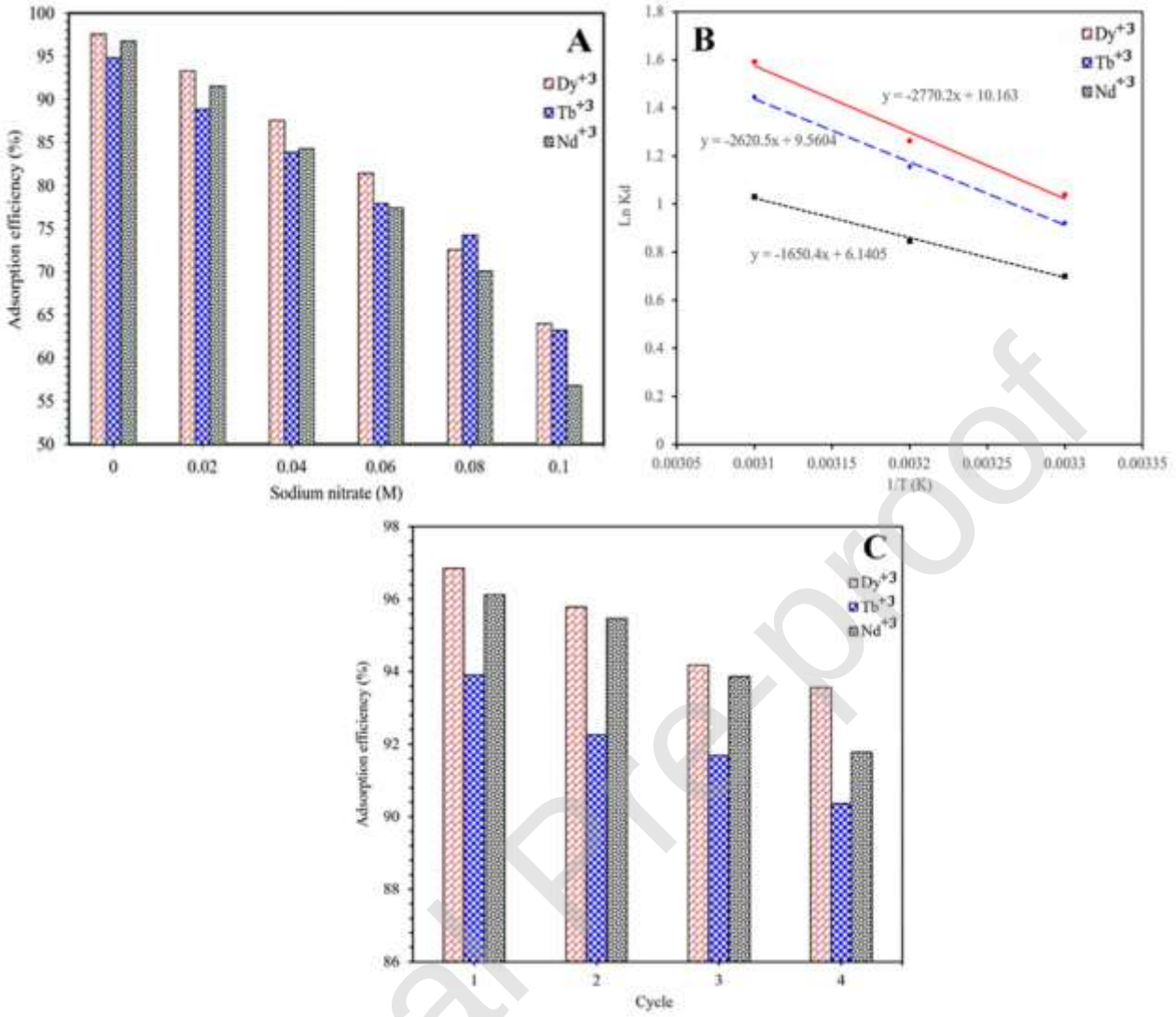

Fig. 11. (A) Ionic strength influence on the REEs adsorption, (B) Ln K_d versus 1/T for ΔH° and ΔS° calculation, and (C) CA-P(P-T-A)-NZFO reusability for the REEs adsorption.

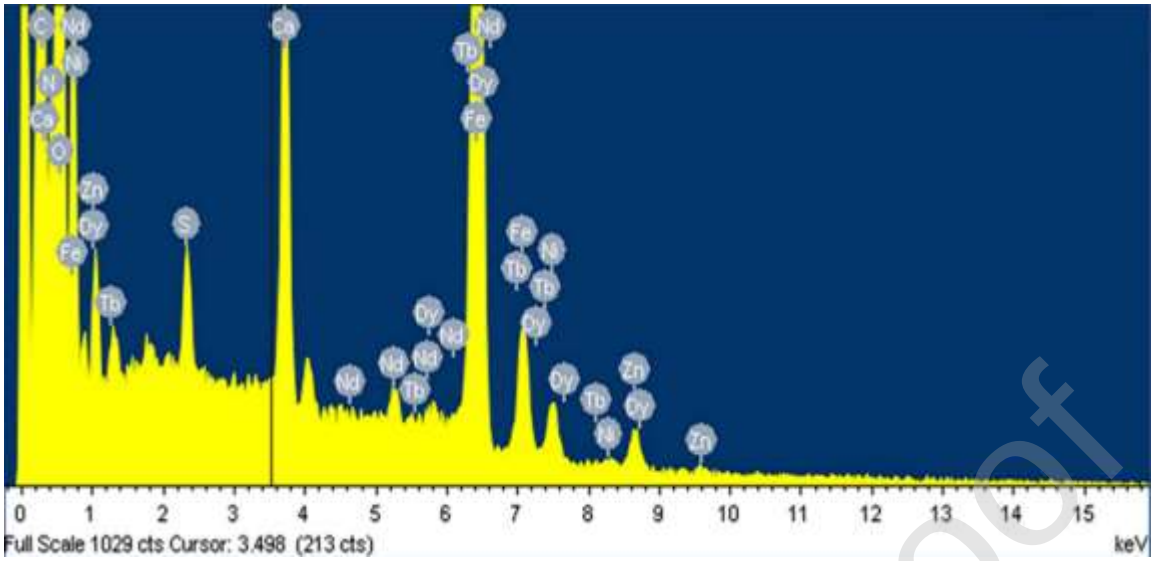

Fig. 12. CA-P(P-T-A)-NZFO EDX spectrum after the REEs adsorption.

Table 1. Kinetic constants for the REEs adsorption onto CA-P-(P-T-A)/NZFO.

		Nd^{+3}	Tb^{+3}	Dy^{+3}
PFO	K_1 (1/min)	0.343	0.314	0.329
	q_e (mg/g)	45.38	44.69	45.37
$q_t = q_e\ (1 - \exp^{-K_1 t})$	R^2	0.8249	0.8927	0.8794
	χ^2	6.67	4.58	5.03
PSO	K_2 (g/mg min)	0.01274	0.01158	0.01195
	q_e (mg/g)	48.05	47.43	48.13
	h (mg/g min)	29.41	26.05	27.68
	(initial adsorption rate) = $K_2 q_e^2$			
$q_t = K_2 q_e^2 t/1 + K_2 q_e t$	R^2	0.9878	0.9974	0.9964
	χ^2	0.46	0.11	0.15
IPD	K_i (1/min)	9.58	9.98	9.88
	R^2	0.8999	0.8708	0.8745
$q_t = K_i t^{0.5} + C$	χ^2	3.81	5.52	5.24

Table 2. Isotherm constants for the REEs adsorption onto CA-P(P-T-A)-NZFO.

		Nd^{+3}	Tb^{+3}	Dy^{+3}
Langmuir	b (L/mg)	0.88	0.199	0.364
	q_m (mg/g)	71.44	98.34	99.91
$q_e = \frac{b\ q_m\ C_e}{(1+bC_e)}$	R_L (dimensionless factor) = $\frac{1}{1+bC_i}$	0.004	0.016	0.009
	C_i: the highest initial metal concentration			
	R^2	0.9563	0.8428	0.7989
	χ^2	8.4	112.03	157.44
Freundlich	K ($mg^{1-1/n}\ L^{1/n}/g$)	44.4	36.58	43.18
	n	9.85	4.91	5.54
	R^2	0.8534	0.9812	0.9877
$q_e = K\ C_e^{1/n}$				
	χ^2	28.24	13.37	9.64

Table 3. Adsorption capacity comparison of different adsorbents for the REEs adsorption.

Adsorbent	q_m (mg/g)			Reference
	Nd^{+3}	Tb^{+3}	Dy^{+3}	
Fe_3O_4-C_{18}-chitosan-DETA	27.1		28.3	[35]
EDTA functionalized chitosan	74			[36]
Phosphonic acid functionalized silica microspheres	45			[37]
γ-Fe_2O_3-NH_4OH@SiO_2 (APTMS)			23.2	[38]
Cellulose functionalized with thiourea	73			[39]
MIL-101-PMIDA	70.9			[40]
A layered thiostannate, $(Me_2NH_2)_{1.33}(Me_3NH)_{0.67}Sn_3S_7 \cdot 1.25H_2O$ (FJSM-SnS)	126			[41]
Oxidized multi-walled carbon nanotubes			78.12	[42]
Lanthanide-ion imprinted polymers	126.5			[43]
Macroporous polymeric resin (TVEX-PHOR)		24.93		[44]
TA-MWCNTs		8.55		[45]
PAAm–YZ		42.9		[46]
Poly(acrylamide-expanded perlite) [P(AAm-EP)]		118.3		[47]
P(HEMA–Hap)		109.66		[48]
Poly(amidoxime-hydroxamic acid)		125		[49]

resins				
CaHAP/NF		130.43		[50]
Acryloyl–phenyl thiourea		74.23		[51]
Hybrid Lewis base ligands functionalized alumina-silica			125.4	[52]
CA@Fe_3O_4 NPs	41			[53]
11-Molybdo-vanadophosphoric acid supported on Zr modified mesoporous silica SBA-15			50	[54]
MPS (22 nm)-2NH-2COOH			44.8	[55]
o-CNCs/GO-IIPs			48.14	[56]
Imprinted mesoporous silica materials			22.33	[57]
CA-P(P-T-A)-NZFO	72.49	108.82[a]	113.08[a]	This study

[a] Calculated from Freundlich isotherm

Table 4. Temperature influence on the REEs (90 mg/L) adsorption and the calculated thermodynamic parameters.

		Adsorption efficiency (%)		
Temperature (°C)		Nd^{+3}	Tb^{+3}	Dy^{+3}
25		61.71	66.79	69.33
35		65.10	71.78	73.90
45		69.15	77.25	79.73
Thermodynamic parameters				
		Nd^{+3}	Tb^{+3}	Dy^{+3}
ΔH° (kJ/mol)		13.72	21.78	23.03
ΔS° (kJ/mol K)		0.051	0.079	0.084
	Temperature (°C)			
ΔG° (kJ/mol)	25	-1.736	-2.284	-2.574
	35	-2.168	-2.961	-3.236
	45	-2.725	-3.823	-4.211